Polymer Chemistry

ROYAL SOCIETY OF CHEMISTRY

PAPER

View Article Online
View Journal | View Issue

Cite this: *Polym. Chem.*, 2025, **16**, 4996

Synthesis of fluorinated phenylene-alkoxybenzothiadiazole polymer (PDTBTBz-2F$_{anti}$) by DHAP

William Dupont, [a] Tristan Marcoux St-Pierre, [a] Louis-Philippe Boivin, [a] Mathieu Mainville, [a] Mario Leclerc, *[a] Paul A. Johnson *[a] and David Gendron *[a,b]

Received 7th October 2025,
Accepted 4th November 2025

DOI: 10.1039/d5py00957j

rsc.li/polymers

Conjugated polymers have garnered significant attention in the field of organic photovoltaics (OPVs) due to their lightweight, flexibility, and tunable properties. However, challenges related to scalability, environmental impact, and batch-to-batch reproducibility still hinder their commercial viability. In this work, we present a new synthesis route for the high-performance polymer PDTBTBz-2F$_{anti}$, known for achieving power conversion efficiencies (PCEs) of up to 9.8% in organic solar cells (OSCs) when paired with PC$_{71}$BM. Our approach replaces conventional Stille polymerization, which relies on toxic organotin compounds, with direct (hetero)arylation polymerization (DHAP), a greener alternative that reduces synthetic steps and hazardous by-products. Additionally, the alkoxybenzothiadiazole unit was partially sourced from biomass. To identify the route yielding a material most comparable to the reference polymer, two polymerization pathways employing different monomers were explored. Organic solar cells fabricated with the resulting materials confirmed that one pathway produced higher-quality polymers. Complementary density functional theory (DFT) calculations provided insight into potential structural defects, which were later supported by experimental findings. Finally, the optimized DHAP pathway was evaluated under continuous flow conditions, to further investigate this synthetic methodology.

Introduction

In recent decades, conjugated polymers and other organic semiconductors have emerged as promising candidates for the development of cost-effective, energy-efficient, and environmentally sustainable electronic devices. Among their many applications, organic solar cells (OSCs) stand out as a lightweight, flexible, and portable power source for modern electronics.[1] However, despite their potential, transitioning from laboratory research to large-scale industrial production poses significant challenges.[2,3] These challenges include the reliance on petroleum-derived compounds, large environmental footprints, complex synthetic procedures, and difficulty in scaling laboratory processes to industrial manufacturing.[4,5]

One of the primary challenges in the industrial production of π-conjugated polymers is the lack of reproducibility across different batches when using conventional batch reactors during scale-up operation.[6–8] This lack of reproducibility is often linked to inconsistent heat transfer and agitation.[9] Alternative process-intensification strategies, such as continuous flow (CF) synthesis, have been proposed to address some of these limitations by enabling better control of reaction parameters and simplifying scale-up.[9–11] While CF methods can provide advantages such as more uniform reaction conditions and easier monitoring, some types of reactions remain complex to adapt, which can limit its broader implementation into the field of conjugated polymers.

In this study, we explore the synthesis of a specific performing conjugated polymer, PDTBTBz-2F$_{anti}$, which has previously been applied in organic photovoltaic (OPV) devices.[12] The benzothiadiazole moiety used in its architecture can be prepared by an added-value compound from biomass (biobased vanillin), reducing the material dependence on petrochemicals.[13–15] When used in bulk heterojunction (BHJ) architectures with the fullerene derivative PC$_{71}$BM, PDTBTBz-2F$_{anti}$ has achieved a power conversion efficiency (PCE) of 9.8%.[16] This high efficiency is attributed to the polymer's donor–acceptor design, featuring alternating fluorinated-thiophene and alkoxy-benzothiadiazole units that enhance molecular ordering and charge mobility.[16]

Previously, PDTBTBz-2F$_{anti}$ was synthesized using Stille-coupling polymerization, a method that employs toxic tin derivatives and produces stoichiometric amounts of hazardous organotin by-products.[16] Traditional polymerization methods,

[a]*Université Laval, Département de Chimie, Québec City, Québec G1V 0A6, Canada. E-mail: mario.leclerc@chm.ulaval.ca, paul.johnson@chm.ulaval.ca, david.gendron.3@ulaval.ca*
[b]*Cégep de Thetford, Kemitek, Thetford Mines Québec, G6G 0A5, Canada. E-mail: dgendron@kemitek.org*

such as Stille or Suzuki cross-coupling reactions, often involve multiple synthetic steps, toxic reagents, and poor atom economy, which limit their scalability and environmental sustainability.[4] To address these issues, direct (hetero)arylation polymerization (DHAP) has been developed.[3] This method eliminates the need for functionalization steps involving organometallic reagents by coupling aromatic (hetero)aryl halides with (hetero)aromatic C–H bonds, producing benign acid by-products.[17] However, it can lead to more defects than the other polymerization methods, since it can produce unwanted C–C bond formations if multiple reactive C–H bonds are present on the monomers.[18] The DHAP mechanism involves the activation of aromatic C–H bonds *via* a concerted metalation–deprotonation step (CMD), where activation of adjacent positions induces irregular couplings.[19] Using density functional theory (DFT) calculations, it is possible to estimate the Gibbs free activation energy (ΔG_{cmd}, kcal mol^{-1}) of every activable C–H bond.[20] These calculations provide insights into the selectivity and reactivity of the monomers under investigation. These theoretical results can complement and guide the interpretation of experimental outcomes, offering an understanding of the polymerization pathway behaviour.

Here, we report the first DHAP synthesis of PDTBTBz-2F$_{anti}$ using a partially biobased monomer and systematically compare two complementary coupling pathways (pathway 1 and pathway 2) that lead to the same repeating unit. This comparative analysis highlights how the choice of monomer architecture influences reaction kinetics, defect formation, and the resulting material properties. After identifying the most efficient route in terms of yield, molar mass, and performance in OSCs, we further assessed its scalability by adapting the selected DHAP pathway to continuous flow conditions.

Results and discussion

To establish the optimal DHAP methodology for the synthesis of PDTBTBz-2F$_{anti}$, we first needed to investigate synthetic routes to achieve properties comparable to the reference material. Two distinct DHAP pathways were explored: pathway 1, utilising monomers M1 and M2, wherein thiophene spacers were attached on the difluorophenyl moiety leading to polymer P1, and pathway 2, employing monomers M3 and M4, with thiophene spacers positioned on the benzothiadiazole unit, leading to polymer P2 (Fig. 1). For comparative purposes, PDTBTBz-2F$_{anti}$ was synthesised *via* Stille coupling (pathway 3, monomers M5 + M2) according to previously reported procedures, with slight modifications to the heating rate during the microwave-assisted polymerisation, leading to polymer P3.[16]

Monomer M1 was obtained *via* Pd-catalyzed direct hetero arylation (DHA) between monomer M4 and thiophene. The synthesis of monomer M2 was carried out as reported in the literature, starting from biomass-derived vanillin.[13] By incorporating a biomass-derived precursor and side chains, the

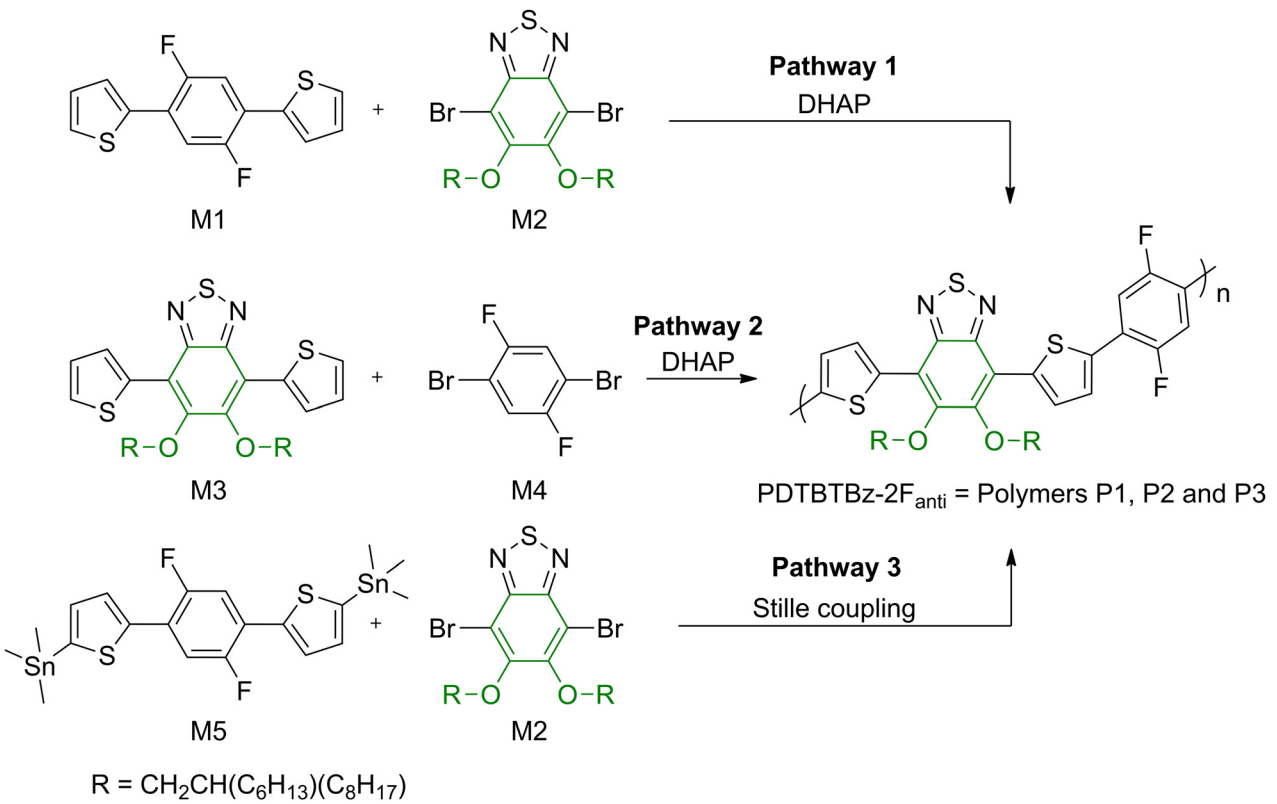

Fig. 1 Synthetic pathways for the preparation of PDTBTBz-2F$_{anti}$ *via* DHAP (pathway 1 and 2) and reference PDTBTBz-2F$_{anti}$ obtained *via* Stille coupling (pathway 3).

overall biobased atom content of the polymers ($\%_{bioT}$) reaches 79% (in green, Fig. 1). However, when considering the more reliable metric ($\%_{bioC}$), which accounts only for the atoms within the conjugated backbone, the biobased content corresponds to 20% for all polymers.[14]

Monomer M3 was synthesized through a DHA coupling between monomer M2 and thiophene.[21] Monomer M4, 1,2-dibromo-4,5-difluorobenzene, was purchased commercially from Combi-Blocks and used without further purification. The last monomer used in this study, monomer M5, was obtained by stannylation of monomer M1 using *n*-butyllithium, followed by the addition of trimethyltin chloride. The detailed synthetic procedures and characterization for monomers and polymers (including ^{1}H and ^{13}C NMR (Fig. S1–S8)) are outlined in the SI.

As mentioned earlier, DHAP can lead to a higher level of defects compared to Stille coupling, due to the unintended activation and coupling of reactive C–H bonds.[19] For both DHAP pathways, DFT calculations were performed to determine the Gibbs free activation energy (ΔG_{cmd}, kcal mol^{-1}) associated with the C–H bonds of the monomers under study, namely monomers M1, M3, and M4 (Fig. 2). Additionally, calculations were carried out for the C–H bonds on the compound resulting of the coupling between a thiophene unit and M4 (M4-Th, Fig. 2). Since monomer M2 contains no aromatic C–H bonds, it cannot contribute to defects arising from unwanted C–H activation.

Before the activation energy calculations, conformational analyses were conducted for monomers M1 and M3, and the compound M4-Th. The values reported in Table 1 correspond to the lowest activation energies obtained among every conformer evaluated, which mainly differ in the orientation of the thiophene spacers.

Interestingly, both monomers M1 and M3 exhibit comparable activation energies for the Hα and Hβ positions (12.3 and 16.6 kcal mol^{-1} for monomer M1 *vs.* 12.4 and 17.0 kcal mol^{-1} for M3, respectively). More importantly, the difference between the activation energies ($\Delta\Delta G_{cmd}$, kcal mol^{-1}) for the two positions is 4.3 kcal mol^{-1} for monomer M1 and 4.6 kcal mol^{-1} for monomer M3. In the literature, $\Delta\Delta G_{cmd}$ is often used as an indicator of a monomer's tendency to generate polymers with a higher defect content. The observed tendency is that a lower $\Delta\Delta G_{cmd}$ leads to a higher content of β-defects, since the likelihood of coupling at the unwanted Hβ position is increased.[22]

Therefore, considering the similar $\Delta\Delta G_{cmd}$ values obtained for monomers M1 and M3, it can be anticipated that the occurrence of β-defects should be comparable for both monomers. When comparing the two polymerization pathways (pathway 1 employing monomers M1 and M2, and pathway 2 employing monomers M3 and M4), no significant difference in the β-defects content is expected. This suggests that both strategies should yield materials with a similar level of structural regularity regarding β-defects incorporation.

However, in pathway 2, when considering the activation energy of Hϕ on monomer M4 (9.8 kcal mol^{-1}) compared to the desired Hα of monomer M3 (12.4 kcal mol^{-1}), it becomes apparent that this lower value could pose a risk of unintended C–H bond activation. The resulting $\Delta\Delta G_{cmd}$ of M4 of −2.6 kcal mol^{-1} could potentially lead to non-selective couplings and would result in a polymer with a higher defect content. By contrast, pathway 1 presents a smaller though still notable risk of non-selective coupling: the $\Delta\Delta G_{cmd}$ between the Hϕ (10.9 kcal mol^{-1}) and Hα (12.3 kcal mol^{-1}) of monomer M1 is −1.4 kcal mol^{-1}. Although this energy gap is less pronounced, branching at the ϕ-position remains possible, albeit less likely than in pathway 2.

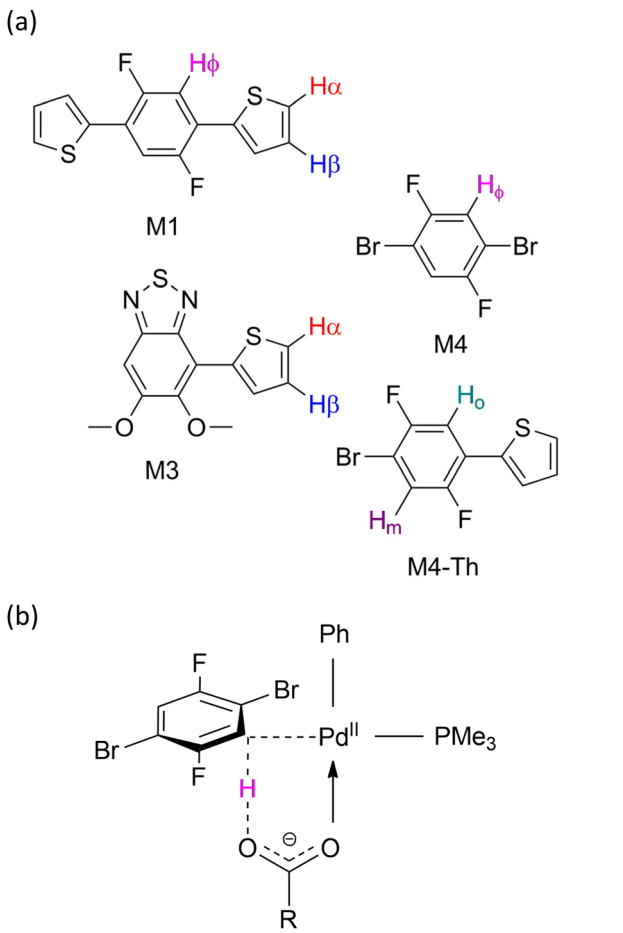

Fig. 2 (a) Representation of the structures of monomers M1, M3 and M4 used for the C–H activation energy DFT modelling, (b) represention of the CMD transition step modelled by DFT.

Table 1 Computational values of C–H bonds activation energies for monomers M1, M3 and M4

Monomer	Activable position	ΔG_{cmd} (kcal mol^{-1})
M1	Hα	12.3
	Hβ	16.6
	Hϕ	10.9
M3	Hα	12.4
	Hβ	17.0
M4	Hϕ	9.8
M4-Th	Ho	8.7
	Hm	10.6

One major source of defects in pathway 2 arises after the first coupling between M3 and M4. When comparing the activation energy of the desired Hα on monomer M3 (12.4 kcal mol^{-1}) with that of the Ho position on M4-Th (8.7 kcal mol^{-1}), the resulting $\Delta\Delta G_{cmd}$ is −3.7 kcal mol^{-1}. This difference indicates a strong likelihood of unwanted coupling at the Ho position.

Overall, DFT calculations serve as a valuable theoretical tool for polymer chemists to more efficiently identify monomers with a reduced risk of defect formation in the final material. Based on computational findings, we anticipated that pathway 1 would yield polymers of higher quality in terms of structural integrity. These theoretical studies were later supported by experimental observations.

DHAP batch synthesis

The investigation of DHAP polymerization conditions for the synthesis of PDTBTBz-2F_{anti} began using the following reaction conditions: the respective monomers (varies between pathway 1 and pathway 2, Fig. 1), tris(2-methoxyphenyl)phosphine as the ligand, pivalic acid, cesium carbonate as the base, and palladium(II) acetate as the precatalyst (Table S1). With this initial result (Table S1, entry 1), cesium carbonate was replaced with the more cost-effective potassium carbonate to reduce synthesis costs and improve suitability for larger-scale continuous flow polymerization.[23] The base equivalents were also increased to evaluate their effect on the reaction outcome. Although the average molar masses increased with higher base loading, excessive amounts (>12 equiv.) led to reduced magnetic stirring efficiency. To overcome this limitation, a biphasic approach was investigated to increase the base availability without impairing agitation.[24] All tested polymerization conditions are detailed in the SI.

The best synthetic conditions tested for polymers P1 and P2 were accomplished utilizing Grenier's biphasic DHAP methodology.[25] The reaction system consisted of a saturated aqueous solution of potassium carbonate and an organic phase containing the respective monomers, tris(2-methoxyphenyl)phosphine as the ligand, pivalic acid, and palladium(II) acetate as the precatalyst. Under these conditions, polymer P1 was obtained after 48 hours with a yield of 72% (Table 2). In the case of polymer P2, longer reaction times (48 h) resulted in the formation of an insoluble material. To maintain processability, the polymerization duration was reduced to 2 hours before the reaction mixture exhibited total gelation. This modified procedure yielded polymer P2 in 36% yield.

The average molar masses of the synthesized polymers were determined by size exclusion chromatography (SEC), yielding number-average molar masses (M_n) of 26, 23, and 28 kg mol^{-1}, for polymers P1, P2 and P3, respectively (Table 2). It is important to note that all SEC analyses were conducted on the polymer fractions soluble in chloroform following Soxhlet extraction, minimizing the measured dispersity ($Đ$) and ensuring the exclusion of insoluble material, especially for polymer P2, since crosslinking was suspected. While all three polymers exhibit comparable M_n values, notable differences in their $Đ$ were observed. Polymers P1 and P3 demonstrated relatively narrow molar mass distributions with $Đ$ values of 2.2 and 2.0, respectively. However, polymer P2 displayed a broader distribution with a dispersity of 4.8, suggesting a less controlled polymerization leading to higher defect content or potential cross-linking occurring during the synthesis.[23]

NMR spectroscopy was performed on all three polymers, P1, P2, and P3, in TCE-d_2 at 90 °C, to confirm their chemical structure and assess the presence of possible structural defects (Fig. S9–S11). Starting with polymer P3, the distinct end-group signal of the trimethylstannyl moiety is clearly observed at 0.49 ppm (Fig. S11), consistent with the polymerization method. The aromatic region shows the expected resonances associated with the thiophene (8.38, 7.71 ppm) and phenylene unit (7.61 ppm), in agreement with the targeted backbone structure.

Regarding polymers P1 and P2, both obtained *via* DHAP, notable difference between the two spectra arises. The spectrum of P1 displays the expected well-defined aromatic resonances at 8.38, 7.71, and 7.61 ppm (Fig. S9), attributable to the regular repeating structure. Polymer P2, however, exhibits broader and more numerous signals across the aromatic region (6.5–8.5 ppm) (Fig. S10). The broadening is indicative of increased structural heterogeneity. These structural irregularities are consistent with the broader dispersity of polymer P2 and possibly arise from branching defects mentioned earlier.

The signal of the aliphatic side chain proton at 4.13 ppm on polymers P2 and P3 spectrum displays a notable shouldering at 4.06 ppm could indicate defects link to homo-coupling or irregular branching. The absence of this shouldering on polymer P1 spectrum indicate a more regular coupling pattern consistent with the lower $\Delta\Delta G_{cmd}$ discussed above.

Table 2 Optical, thermal, physical and electrochemical properties of P1, P2 and P3

Polymers	$\lambda_{max,\ sol}$ [a] (nm)	$\lambda_{max,\ film}$ [b] (nm)	HOMO[b] (eV)	LUMO[b] (eV)	$E_{g\ opt}$ [c] (eV)	$E_{g\ elec}$ (eV)	M_n (kg mol^{-1})	$Đ$	T_d (°C)	T_f (°C)	Yield (%)
P1	547	563	−5.56	−3.37	1.93	2.19	26	2.2	326	141	72
P2	508	534	−5.71	−3.54	1.97	2.17	23	4.8	327	142	36
P3	549	564	−5.53	−3.35	1.92	2.18	28	2.0	326	139	81

[a] In solution ($CHCl_3$). [b] Obtained from the onset of the oxidation and reduction curves of a film on a platinum electrode in 0.1 M tetrabutylammonium tetrafluoroborate solution in CH_3CN and were calculated according to $E_{HOMO} = -(4.80 + E_{ox\ onset})$ eV and $E_{LUMO} = -(4.80 + E_{red\ onset})$ eV, in which $E_{ox\ onset}$ and $E_{red\ onset}$ represent oxidation and reduction onset potentials of the polymers *versus* the half-wave potential of a ferrocene/ferrocenium redox couple. [c] The optical bandgaps ($E_{g\ opt}$) were calculated from the film absorption onset.

Additionally, phase transfer agents were evaluated in biphasic polymerization reactions to assess their potential to facilitate interfacial transport and enhance reactivity.[25] However, all tested additives (Table S1, entries 11–13) were found to inhibit the polymerization.

Optical and electrochemical properties

Table 2 reports the optical, thermal, physical and electrochemical properties of polymers P1, P2 and P3. The optical properties of polymers P1–P3 were investigated using UV-Visible spectroscopy in solution in chloroform at room temperature and in thin films (Fig. 3). In solution, polymer P1 exhibited an absorption maximum ($\lambda_{max,\ sol}$) at 547 nm, while polymers P2 and P3 showed maximum absorptions at 508 nm and 549 nm, respectively. In the solid state, bathochromic shifts were observed for all polymers, with thin-film absorption maxima ($\lambda_{max,\ film}$) at 563 nm (P1), 534 nm (P2), and 564 nm (P3). This red shift can be attributed to enhanced π–π stacking and molecular ordering in the solid state.[26] The optical bandgaps ($E_{g\ opt}$) were calculated from the absorption onset of the polymer thin films, resulting in values of 1.93 eV (P1), 1.97 eV (P2), and 1.92 eV (P3).

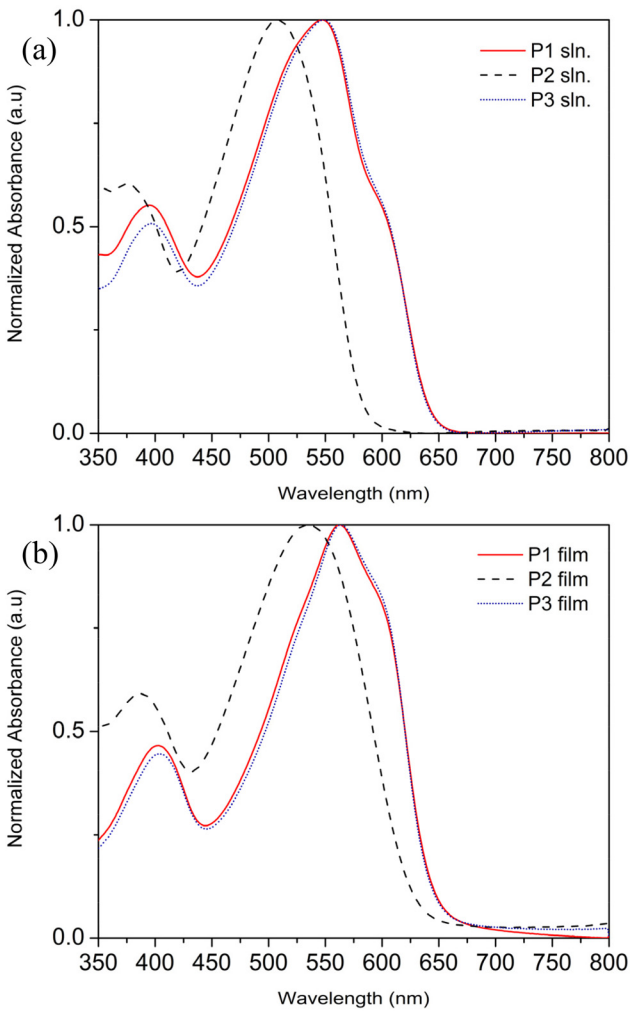

Fig. 3 Normalized UV-Visible absorption spectra of PDTBTBz-2F$_{anti}$ polymers P1, P2 and P3 synthesized: (a) in $CHCl_3$ solutions (b) in thin films.

Interestingly, the UV-Vis absorption spectra reveal distinct optical signatures for polymer P2 compared to polymer P3. In solution (Fig. 3(a)), polymers P1 and P3 show a well-defined vibronic structure, characterized by a prominent primary peak (A_{0-1} transition) and a lower-energy shoulder (A_{0-0} transition) around 610 nm.[27] This pronounced vibronic fine structure indicates strong intramolecular interactions and suggests a more rigid, planar backbone, hinting at possible aggregations.[28] In contrast, polymer P2 displays a less resolved vibronic pattern and a null A_{0-0} to A_{0-1} peak ratio, reflecting lower intramolecular order and intermolecular interactions.[29]

In thin films (Fig. 3(b)), both polymers P1 and P3 retain their characteristic absorption profiles with notable differences in their vibronic features. They both display an increase A_{0-0} to A_{0-1} peak ratio, indicating enhanced intermolecular ordering and improved π–π stacking interactions in the solid state.[30] This suggests that polymer P1 maintains conformational rigidity and planar backbone alignment upon film formation, which is beneficial for charge transport properties.[31] As for polymer P2, it also exhibits less pronounced vibronic features, indicating a more amorphous packing arrangement in the solid state.[30]

To support the observation of aggregation of polymers P1 and P3 in solution, UV-vis characterizations were performed at various temperatures in *ortho*-dichlorobenzene (ODCB) for all polymers. The temperature-dependent UV-Vis absorption spectra of polymers P1 and P2 are shown in Fig. 4(a) and (b), respectively. The polymer P3 temperature-dependent UV-Vis absorption spectrum is shown in Fig. S12. For polymer P1, increasing the temperature from 30 °C to 90 °C leads to a decrease in the intensity of the A_{0-0} absorption band, with a slight hypsochromic and hypochromic shift of the absorption maxima, hinting at lower conjugation caused by backbone twisting.[32] This diminution of the A_{0-0} peak with temperature suggests a disruption of the molecular packing and a reduction in intermolecular π–π stacking interactions.[33] Thus, the temperature sensitivity of the A_{0-0} band indicates that polymer P1 forms aggregates stabilized by strong intermolecular interactions at lower temperatures, which are progressively disassembled upon heating. This behaviour also reflects the presence of a more regular backbone conformation in polymer P1.[30] In contrast, the absorption spectra of polymer P2 (Fig. 4(b)) exhibit minimal changes across the same temperature range, which supports the claim of weaker intermolecular interactions and a more amorphous packing arrangement, consistent with a less ordered molecular structure.[33,34] A photograph illustrating the colour shift of the polymer P1 solution is provided in the SI (Fig. S13).

To gain further insight into the polymer's optical signatures, emission spectra were also recorded in chloroform solution at room temperature for polymers P1, P2 and P3 (Fig. S14–S16). Excitation at the absorption maxima in solution leads to emission spectra for polymer P1 (Fig. S14) and P3

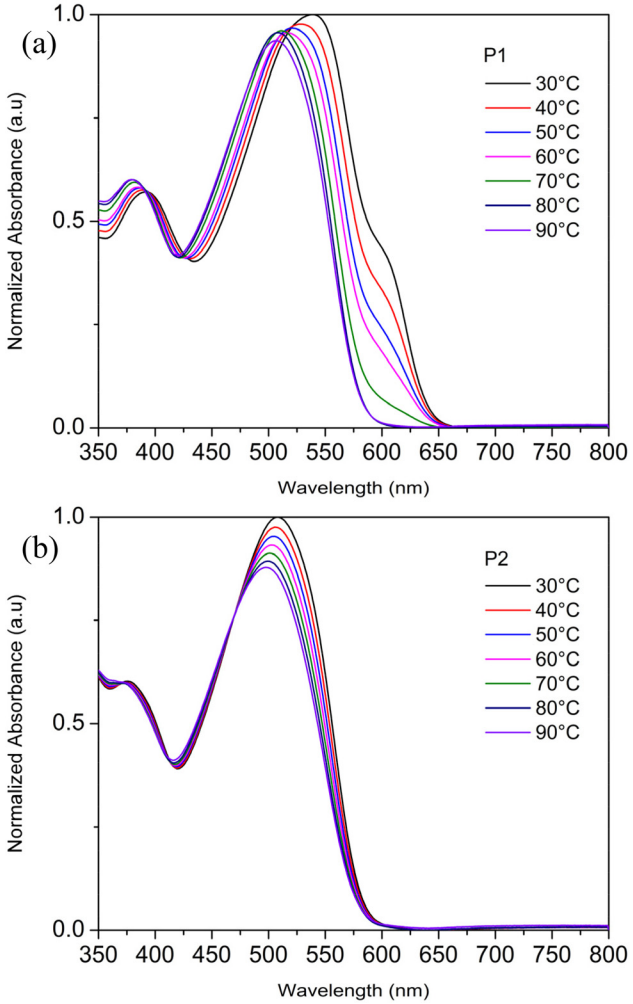

Fig. 4 Temperature-dependent UV-Visible absorption spectra of PDTBTBz-2F_{anti} polymers in *ortho*-diclorobenzene (ODCB) solution measured at temperatures ranging from 30 °C to 90 °C: (a) polymer P1 (b) polymer P2.

(Fig. S16) exhibiting a distinct second emission band at around 712 nm, linked to their strong π–π interactions. In contrast, polymer P2 only displays a small shoulder effect (Fig. S15).

The frontier molecular orbital energy levels were determined *via* cyclic voltammetry measurements (Fig. S18–S20). The highest occupied molecular orbital (HOMO) and lowest unoccupied molecular orbital (LUMO) energy levels were estimated from the onset potentials of the oxidation and reduction waves, respectively. The electrochemical band gaps ($E_{g\ elec}$) were determined, from thin films, to be 2.19 eV, 2.17 eV, and 2.18 eV for polymers P1, P2, and P3, respectively. These values were found to be consistently larger than their optical counterparts ($E_{g\ opt}$, Table 2), a common observation in conjugated polymers due to the contribution of exciton binding energy in electrochemical measurements.[35]

Polymer P3 exhibits optical and electrochemical properties that are highly consistent with those previously reported for the same polymer.[16] Notably, $\lambda_{max,\ film}$ matches exactly the value reported in the literature, despite the lower molar masses obtained in our case. This suggests that the key electronic features of the polymer backbone are preserved even at reduced chain lengths.

Thermal properties

The thermal behaviour of the synthesized polymers (Table 2) was investigated by thermogravimetric analysis (TGA) and differential scanning calorimetry (DSC). TGA analysis revealed that all polymers (P1, P2 and P3) exhibit high thermal stability, with decomposition temperatures (T_d, 5% weight loss) above 300 °C (P1: 326 °C, P2: 327 °C, P3: 326 °C) under a nitrogen atmosphere, indicating their suitability for device applications (Fig. S21–S23).

Differential scanning calorimetry (DSC) analysis (Fig. S21–S23) resulted in no apparent glass transition (T_g). However, distinct endothermic peaks associated with a melting transition (T_f) at 141 °C, 142 °C and 139 °C for polymers P1, P2 and P3, respectively, were detected. This transition around 140 °C, is significantly lower than the melting temperature reported for PDTBTBz-2F_{anti} synthesized by Stille coupling ($T_f \approx 275$ °C).[16] This difference can be attributed to the lower molecular weights obtained in both the DHAP and Stille syntheses performed in this work compared to the literature values. Reduced chain length typically limits crystalline domain formation, resulting in diminished enthalpy and lower apparent melting temperatures.[36]

Solid-state morphology

The X-ray diffraction (XRD) patterns of thin films of polymers P1, P2, and P3 are presented in Fig. S24. All samples exhibit diffraction features characteristic of semicrystalline conjugated polymers, with a major peak at low scattering angles ($2\theta \approx$ 3–5°) assigned to the (100) lamellar stacking of the side chains and a broader feature around 20–25° associated with π–π stacking between conjugated backbones.[37]

The principal (100) maximum appears at 2θ = 4.54°, 4.21°, and 4.71° for polymers P1, P2, and P3, respectively. Using Bragg's law (with Cu Kα = 1.540598 Å), the lamellar spacings are calculated to be 19.47 Å (P1), 20.97 Å (P2), and 18.74 Å (P3).[14] The slightly larger *d*-spacing and broader profile of P2 indicate a less ordered arrangement, consistent with reduced crystallinity and disrupted sidechain packing caused by a higher density of structural defects. In contrast, polymers P1 and P3 display narrower and more intense (100) peaks, revealing a more uniform lamellar stacking. The nearly identical *d*-spacings of P1 and P3 suggest that the DHAP polymer obtained *via* pathway 1 possesses a level of structural regularity and chain organization comparable to that of the Stille-synthesized polymer.

Importantly, both polymers P1 and P3 exhibit an additional, weaker diffraction feature around $2\theta \approx$ 9.1–9.3°, corresponding to the (200) diffraction. The appearance of this higher-order signal further confirms a more ordered lamellar organization and enhanced stacking for these two polymers.[37]

Such ordering is absent in polymer P2, reinforcing its more amorphous nature and lower degree of crystallinity.

The π–π stacking region $2\theta \approx 20$–$25°$ follows a similar trend: polymers P1 and P3 show better-defined peaks with higher relative intensity, indicative of stronger interchain interactions and improved backbone planarity, whereas P2 presents a broad, low-intensity feature suggesting weaker π–π interactions and higher conformational disorder.

Overall, these results demonstrate that pathway 1 yields a polymer with structural order and semicrystalline morphology comparable to the benchmark Stille material (polymer P3), while pathway 2 produces a less ordered polymer with expanded lamellar spacing and diminished packing coherence.

Organic solar cells

The photovoltaic performances of the synthesized conjugated polymers P1, P2, and P3 were evaluated in bulk heterojunction (BHJ) organic solar cells. This process aimed to investigate the impact of structural differences in polymer P2, in comparison to polymer P1 and the reference polymer, P3. The solar cells were fabricated under ambient conditions, using the same protocol, without any optimization for each material. This ensures that the observed performance trends were primarily influenced by the intrinsic properties of the polymers rather than processing variables. By comparing the power conversion efficiencies (PCEs), open-circuit voltages (V_{oc}), short-circuit currents (J_{sc}), and fill factors (FF) of the devices, we aimed to establish correlations between molecular structure and photovoltaic behaviour. The devices were printed on a glass substrate in inverted architecture corresponding to the following layers (bottom to top): ITO/ZnO/PDTBTBz-2F_{anti}:$PC_{61}BM$/MoO_x/Ag, with PDTBTBz-2F_{anti} serving as the donor polymer and $PC_{61}BM$ as the acceptor (Fig. 5). Details of the device fabrication process and characterisations are provided in the SI. The performance of the organic solar cells under illumination shows similar performance between polymers P1 and P3, whereas polymer P2 exhibits lower efficiency (Table 2). The current density–voltage (J–V) curves and extracted device parameters (J_{sc}, V_{oc}, and FF) indicate that polymers P1 and P3 achieve higher J_{sc} values of 6.39 mA cm^{-2} and 6.43 mA cm^{-2}, respectively, compared to the lower J_{sc} of 3.38 mA cm^{-2} for polymer P2 (Fig. S25). Similarly, the PCEs for polymers P1 and P3 are 2.46% and 2.32%, while polymer P2 shows a reduced PCE of 1.02%. This difference can be attributed to the structural defects in polymer P2 caused by undesired C–H branching, as mentioned earlier, which likely disrupts conjugation and charge transport.[38] Additionally, the higher weight average molar mass (M_w) of polymer P2 (110 kg mol^{-1}) relative to polymers P1 and P3 (both 57 kg mol^{-1}) may have led to the formation of larger polymer domains in the active layer, resulting in poorer phase segregation with $PC_{61}BM$ and inefficient charge dissociation and extraction.[39,40] This broader polydispersity of polymer P2, leading to larger domains in the BHJ, is reflected in the fill factor of the solar cells, which is lower at 0.34, compared to 0.49 and 0.52 for P1 and P3.[40] These results support the hypothesis that the choice of DHAP pathway used for the polymerisation of PDBTBz-2F_{anti} plays a crucial role in determining the structural regularity and photovoltaic performance of the resulting material (Table 3).

It is important to note that these devices were fabricated under ambient conditions and without optimization of processing parameters or active-layer morphology. This likely led to increased exposure to oxygen and moisture during device processing, which are known to negatively affect the PCEs.[41] As such, the efficiencies reported here are intended only for com-

Table 3 Devices characteristics of PDTBTBz-2F_{anti}:$PC_{61}CM$ based OSCs[a]

	J_{sc} (mA cm^{-2})	V_{oc} (V)	FF	PCE (%)
P1	7.06 (6.39)	0.85 (0.81)	0.49 (0.48)	2.93 (2.46)
P2	3.74 (3.38)	0.97 (0.91)	0.33 (0.34)	1.20 (1.02)
P3	6.94 (6.43)	0.87 (0.75)	0.52 (0.48)	3.18 (2.32)

[a] Average values bracketed were obtained from 12 devices.

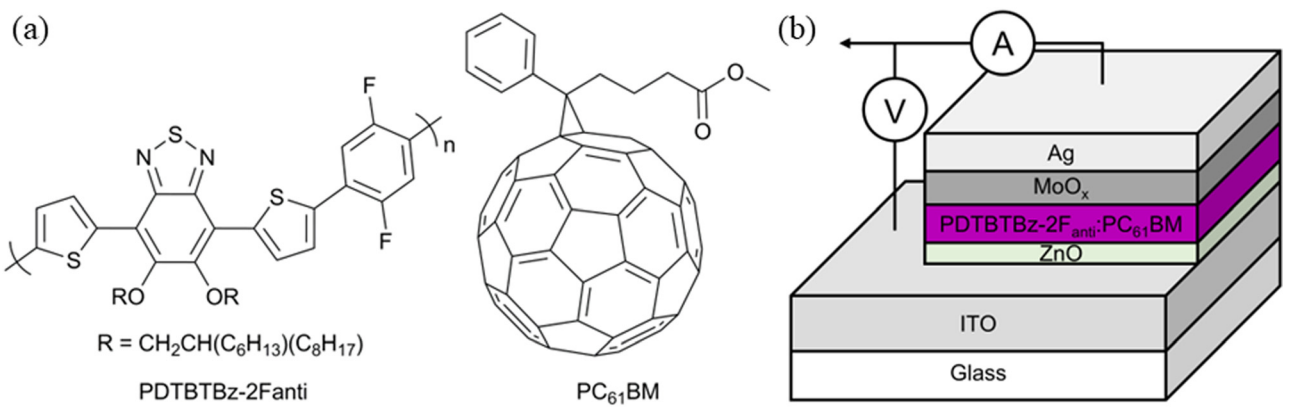

Fig. 5 (a) Chemical structures of PDTBTBz-2F_{anti} and $PC_{61}BM$ fullerene derivative used in the BHJ of the OSCs; (b) schematic representation of the complete bulk heterojunction solar cell device architecture showing the different layers: glass substrate, ITO electrode, ZnO electron transport layer, PDTBTBz-2F_{anti}:$PC_{61}BM$ active layer, MoO_x hole transport layer, and silver top electrode.

parative purposes between the different polymer batches and synthetic pathways. Under optimized conditions and using another fullerene acceptor, the same polymer, although with higher molar mass (M_n = 56 kg mol^{-1}), has previously achieved PCEs of up to 9.8%.[16] Therefore, the lower efficiencies observed in this work should not be interpreted as an intrinsic limitation of the material, but rather as a reflection of the simplified fabrication approach used for this comparative study.

Continuous flow adaptation

With the experimental data confirming the theoretical hypothesis that pathway 1 led to a material with fewer structural defects and closer resemblance to the previously reported polymer P3, we decided to synthesize PDTBTBz-2F$_{anti}$ using a continuous flow (CF) procedure. As introduced earlier, CF offers a more scalable and controllable alternative to traditional batch methods.[11] In CF, reagents are continuously pumped through a heated reactor, ensuring constant reaction conditions such as temperature, residence time, and concentration.

We based our adaptation of PDTBTBz-2F$_{anti}$ continuous flow synthesis on previous works by our group. Grenier *et al.*'s protocol allowed for the preparation of PiIEDOT, an isoindigo and EDOT polymer, in CF by DHAP.[23] Using a column reactor packed with a blend of pivalic acid and cesium carbonate dispersed in diatomaceous earth (Celite(TM) 545 Filter Aid), they achieved reproducible molar masses around 42 kg mol^{-1}. It is noteworthy that the molar mass obtained during traditional synthesis in vials achieved higher molar masses at around 93 kg mol^{-1}.

Other work in the literature, such as by Gobalasingham *et al.*, compared DHAP to Stille coupling for the synthesis of PPDTBT in continuous flow.[9] They reported higher molar masses for the polymer obtained *via* CF-DHAP compared to the one synthesized *via* CF-Stille coupling (60 *vs.* 53 kg mol^{-1}, respectively). This result was achieved using a protocol similar to Grenier *et al.*, which includes the use of a stationary column. A column reactor is employed in all reported instances of DHAP performed in continuous flow to date (heterogeneous CF). Since most HPLC pumps used in continuous flow setups are incompatible with suspensions, reagents that are insoluble in organic solvents must be incorporated into a stationary phase within the column.[42]

Process using column reactor (standard DHAP). The initial test was carried out using a Vapourtec E-series benchtop flow apparatus equipped with a column reactor (15 cm in length, 1 cm inner diameter) packed with cesium carbonate and pivalic acid dispersed in Celite. The remaining reagents (M1, M2, Pd(OAc)$_2$, P(*o*-OMePh)$_3$) were dissolved in dry, degassed toluene ([0.2 M]) and injected into the column using an injection loop at the lowest flow rate permitted by the apparatus (0.1 mL min^{-1}) (Fig. 6). This flow rate provided a residence time of approximately 55 minutes. The pressure was always kept above 2 bars using the back-pressure regulator (BPR) to prevent solvent boiling. An extra pump was utilized to pump

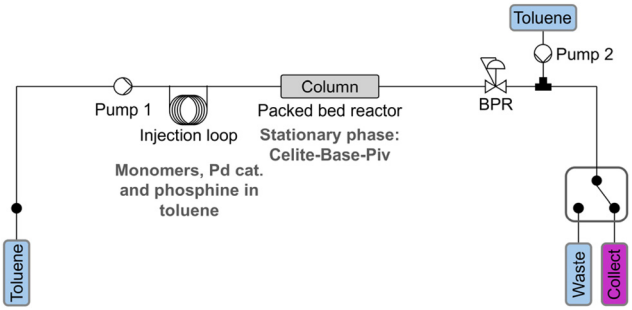

Fig. 6 Continuous flow diagram of the standard DHAP flow synthesis using a column reactor, BPR: back pressure regulator.

fresh toluene after the reactor to avoid precipitation/gelation of the polymer when cooling to room temperature.[43]

All detailed parameters, including stationary phase composition, reaction time, temperature, and reagent concentrations are regrouped in Table S2.

This initial test (Table S2, entry 1) demonstrated that the continuous-flow approach was feasible but required optimization, as only a slight colour change was observed (yellow → orange), and no material could be precipitated or isolated for SEC characterization. Subsequent entries in Table S2 explored various conditions, including a different base (K_2CO_3), various stationary phase compositions, varying residence times, concentrations, and temperatures. To guide the optimization process, UV-Vis characterization of the crude, unpurified reaction mixtures was employed (Fig. S26).

This ultimately led to the preparation of polymer (P4) that could be isolated and purified by Soxhlet washings (methanol followed by acetone) and extracted in hexane. Polymer P4 exhibited a M_n of approximately 7.7 kg mol^{-1} (Table 4), which is lower compared to the polymers synthesized *via* batch processing. The detailed synthetic parameters for its synthesis are compiled in Table S2, entry 9. Polymer P4 was obtained using a stationary phase composed of potassium carbonate, pivalic acid, and a minimal amount of Celite. While Celite is necessary to prevent clogging, it does not contribute to the reactivity of the polymerization process. To extend the residence time and possibly maximize monomer conversion, three columns were connected in series, allowing for an expected reaction time of approximately 3 hours. However, the actual residence time recorded for polymer P4 was unexpectedly longer (300 min). This discrepancy is attributed to polymer adhesion to the stationary phase, resulting in tailing and increased dilution, which in turn reduces reactivity.[23] This tailing negatively impacts the reproducibility and continuous aspect of the

Table 4 Summary of characterizations for polymer P4 and P5 obtained *via* continuous flow procedures

Polymer	Reactor	M_n (kg mol^{-1})	$Đ$	Yield (%)
P4	Packed-bed	7.7	2.9	76
P5	Tubular	2.1	1.4	—

synthesis, since a new stationary phase mixture needs to be prepared and hand-packed. A similar issue was reported by Grenier *et al.*[23]

When performing polymerization reactions in a continuous flow system using a column reactor, the injection volume of the reaction mixture plays a critical role in determining the overall reactivity and yield. Specifically, when a small reaction volume is introduced into the column, the inherent dispersion caused by convective and diffusive currents leads to a broadening of the reaction in the column.[8,44] This manifests as dilution of the leading (head) and tailing (tail) edges of the reaction (Fig. 7).[45]

This dilution effect at the head and tail of the injection plug reduces the local concentration of reactants and catalysts, thereby lowering the reactivity in these regions, negatively impacting the polymerization yield and molar masses obtained.[23]

To remedy this issue, the injection volume can be increased. A larger injected solution leads to a larger central reactive zone (body), where the concentrations remain high enough for effective cross-coupling. The relative influence of the diluted head and tail regions is then minimized.[23]

Knowing this, this last attempt (Table S2, entry 9) was performed on a scale six times as large. However, with the adhesion of higher molar mass material in the column, the reaction was stopped after 300 minutes, even though the solution exiting from the column reactors was still coloured. After the reaction and disassembly of the apparatus, the stationary phase remained stained by the material.

These results highlight an intrinsic limitation of heterogeneous CF polymerizations: progressive adhesion of high-molecular-weight material to the stationary bed leads to residence-time dispersion, tailing, and loss of reproducibility. Overcoming these issues and obtaining a truly continuous system applicable on various π-conjugated materials synthesis will require redesigning reactors and exploring new synthetic conditions.

Process using a tubular reactor (biphasic DHAP). As mentioned earlier, DHAP synthesis has previously been adapted for continuous flow processes. However, all reported methods to date utilize column reactors containing a stationary phase composed of reagents insoluble in organic solvents.[42]

The use of a stationary phase, however, introduces several challenges, including clogging, high-pressure, limited mass and heat transfer, and non-uniform reaction conditions along the reactor's length.[9,46] These limitations not only reduce reaction efficiency but also hinder process scalability, resulting in inconsistent yields and production downtimes. These downtimes are associated with the need to replace the stationary phase in the column reactor with a fresh one. To address these issues, the biphasic system is designed to eliminate the need for a stationary phase. In this homogeneous approach, all reagents are used in solution, thus avoiding some of the clogging and pressure issues typical of packed columns, but introduces other challenges related to residence-time control and mass-transfer efficiency.

The biphasic DHAP experiment was conducted using the same Vapourtec E-Series continuous-flow system, previously employed for packed-bed column reactions. However, for this setup, the system was equipped with a 10 mL tubular reactor and heated to 110 °C using the integrated air oven of the instrument (Fig. 8).

The biphasic system employed a solution of potassium carbonate (1 g mL^{-1}) in degassed water as the aqueous phase. All other reagents, including the monomers, pivalic acid, phosphine ligand, and the palladium precatalyst, were dissolved in dry, degassed toluene to form the organic phase mixture. Once the reactor system reached thermal and flow equilibrium with both the aqueous base and toluene, the injection of the reagent mixture was initiated *via* a sample injection loop.

As shown in Fig. 8, the dual-pump configuration required for this synthesis meant that the minimum total flow rate was 0.2 mL min^{-1} (pump A 0.1 mL min^{-1} and pump B 0.1 mL min^{-1}). Under these conditions, the residence time within the 10 mL tubular reactor was approximately 50 minutes.

Just as the synthesis was conducted with a stationary phase, the first test led only to a slight colour change of the reacting mixture, indicating that cross-coupling was occurring, but the molar mass remained quite low (less than ~2 kg mol^{-1}). To increase molar mass and overall reactivity, optimization of the reacting conditions was necessary. All detailed experimental details, including temperature, concentration of the organic phase, flow rates and tube reactor volume, are compiled in Table S3.

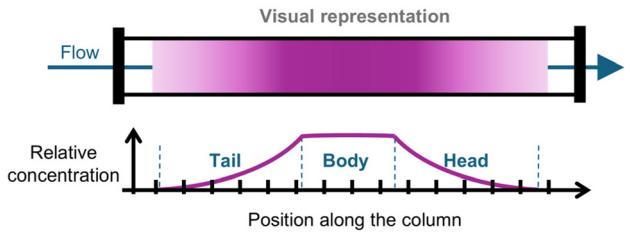

Fig. 7 Representation of the dilution effect during continuous flow synthesis in a column reactor: (top) visual representation of the concentration gradient within the column; (bottom) corresponding relative concentration profile showing the characteristic tail, body, and head regions of the reaction mixture along the column length.

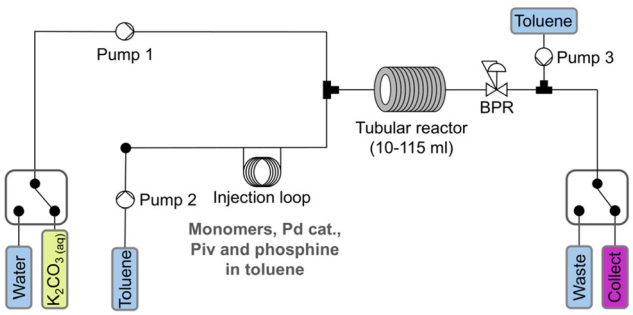

Fig. 8 Continuous flow diagram of the biphasic DHAP flow synthesis using a tubular reactor, BPR: back pressure regulator.

None of the tested conditions resulted in a significant improvement in the molar mass of PPDTBTBz-2F$_{anti}$. Even when employing a larger reactor with an internal volume of 115 mL (corresponding to approximately 100 m of tubing), elevated temperatures (up to 140 °C), and a more concentrated organic phase (up to [0.4 M]), no significant increase in reactivity was observed (Table S3, entry 9). The M_n remained consistently low (2.1 kg mol^{-1}, Table 4, P5), suggesting that only limited cross-coupling was occurring under these conditions.

As both polymers P4 and P5 exhibited low molar masses adjacent to oligomers, no further characterizations were conducted.

The use of two immiscible phases (liquid–liquid) allowed for the formation of a plug flow regime, characterized by the segmented flow of immiscible aqueous and organic phases through the tubular reactor.[47] In this regime, the reaction mixture is composed of alternating slugs of aqueous base and organic solution, forming discrete fluid segments.[48] Each interface between slugs acts as a localized microreactor where the reaction occurs (Fig. 9).

The efficiency of such biphasic systems strongly depends on the interfacial surface area between the two phases. Shorter fluid segments increase the number of interfaces, thereby enhancing the total interfacial surface area available for mass transfer and reaction. Consequently, a plug flow regime with shorter, more frequent slugs is expected to lead to improved reactivity and yields due to the higher total contact area between phases. On the opposite side, longer slugs result in fewer interfaces and reduced interfacial area, which limits the reaction rate.[49] Therefore, controlling slug size through flow rate, viscosity, and phase ratio becomes a critical parameter for optimizing performance in biphasic continuous-flow DArP.

In addition to interfacial surface area, internal fluid dynamics within the slugs also play a key role. At higher flow rates, the increased shear and pressure gradients induce stronger Taylor recirculation currents within each slug.[50] These currents enhance mixing within the slugs and promote more efficient mass transfer across the aqueous–organic interface. This internal circulation accelerates phase exchange and supports more effective catalyst–substrate interactions, thereby increasing the apparent reaction rate.

However, for polycondensation reactions, such as DHAP, the polymer chain growth is nonlinear.[51] Molar mass tends to increase significantly only in the later stages of the reaction as monomer concentration diminishes, and chains grow longer. Therefore, although elevated flow rates promote better interfacial mixing through enhanced Taylor currents, they also reduce the overall residence time in the reactor. If the residence time becomes too short, the reaction is prematurely stopped, leading to a lower M_n. As a result, a balance had to be found between flow rates high enough to ensure strong mixing/good phase segmentation, and low enough to allow sufficient reaction time for high molar mass polymer formation.

Overall, these experiments underline the current challenges of implementing DHAP in both homogeneous and heterogeneous continuous-flow set-up. The reduced molar masses and broad tailing observed for polymers P4 and P5 stem from residence-time dispersion, adhesion, and incomplete conversion. These are all characteristic limitations of polycondensation reactions under flow. These limitations also slow the broader implementation of such setups at larger scales, as precise optimization is required for each specific polymer system due to the strong influence of reaction kinetics on the outcome.

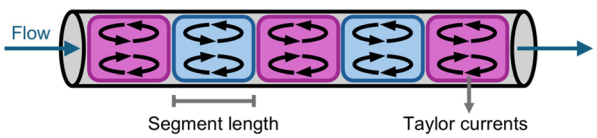

Fig. 9 Representation of biphasic liquid–liquid flow in a tubular reactor alternating immiscible liquid segments with characteristic internal Taylor circulation currents (black arrows).

Conclusions

In summary, partially biobased PPDTBTBz-2F$_{anti}$ was synthesized for the first time *via* DHAP, under both standard and biphasic conditions. Two distinct synthetic pathways (pathway 1 and pathway 2) were explored to identify the strategy yielding a polymer with comparable structural and optoelectronic characteristics to the benchmark material prepared *via* Stille coupling. Among the tested routes, polymer P1 obtained from pathway 1, involving thiophene spacers on the difluorophenyl moiety, proved superior in terms of polymer quality and performance in OSCs. Knowing this pathway was the preferred one, it was then adapted to continuous flow synthesis.

We also demonstrated that DFT calculations effectively predicted the relative reactivity and selectivity of the monomers, allowing for the early identification of potential sources of defects when using pathway 2. The good agreement between computational predictions and experimental results (polymer P2 characterizations) underscores the value of theoretical tools in the design and optimization of monomers for high-performance conjugated polymers.

The synthesis using pathway 1 was conducted in two continuous flow setups, one using packed-bed column reactors (polymer P4), the other one using a tubular reactor for the biphasic adaptation (polymer P5). Although both systems successfully displayed their ability for cross-coupling, neither led to materials with molar masses achieved in traditional batch polymerizations. Nevertheless, the biphasic flow strategy could still be well-suited for materials with inherently faster reaction kinetics, where shorter reaction times with faster flow rates could favour efficient polymer growth.

Altogether, this work highlights how a combination of theoretical calculations, synthetic optimization, biobased monomers and flow processing could contribute to the advancement of greener polymerization reactions for high-performance donor–acceptor polymers for organic electronics.

Experimental section

Measurements

^{1}H and ^{13}C NMR spectra of the monomers were recorded using an Agilent DD2 500 MHz and a Varian Innova 400 MHz spectrometers in the appropriate deuterated solvents at 293 K for the monomers and at 353 K for the polymers. Chemical shifts were reported as δ values (ppm) relative to the residual solvent signals ($CDCl_3$ = 7.26 ppm (^{1}H NMR), 77.00 ppm (^{13}C NMR) and deuterated 1,1,2,2-tetrachloroethane (TCE-d_2) = 6.00 ppm (^{1}H NMR)), coupling constants are given to the nearest 0.5 Hz. UV-Visible absorption spectra in solution ($CHCl_3$) and in thin films (glass substrate) were recorded using a Varian Cary 500 UV-Vis spectrophotometer. Fluorescence spectra in solution ($CHCl_3$) were obtained with a Varian Cary Eclipse. Spectra in solutions were taken with a 1 cm path-length quartz cell, and solid-state spectra were recorded with spin-coated materials on glass substrates. The optical band gaps ($E_{g\ opt}$) of the materials were calculated using the onset of the UV-Vis absorption curves, using the Planck–Einstein relation. The electrochemical cyclic voltammograms were obtained on a Solartron SI 1287. A 0.1 M solution of tetrabutylammonium tetrafluoroborate in acetonitrile protected in an argon atmosphere was used for the measurement. Platinum wires were used as working and counter electrodes. For the reference electrode, a silver wire and a 0.1 M $AgNO_3$ solution was utilized. As an internal standard, the ferrocene·ferrocenium redox couple was used. Electrospray ionization (ESI) high-resolution mass spectrometry (HRMS) was carried out using an Agilent 6210 LC time-of-flight mass spectrometer. Column chromatography was performed with 230–400 mesh silica purchased from Silicycle. Thin-layer chromatography (TLC) was performed on aluminum-backed plates coated with silica gel (thickness = 200 μm). TGA measurements were performed with a Mettler Toledo TGA SDTA 851e under constant nitrogen flow, at a heating rate of 20 °C min^{-1}. The differential scanning calorimetry (DSC) analyses were performed using a Mettler Toledo DSC823e under constant nitrogen flow. Calibration was done using an indium standard. All curves presented were performed as a successive three-step process with an initial heating from −50 °C to 300 °C, a cooling step from 300 °C to −50 °C, to a last heating from −50 °C to 300 °C. The temperature scanning rate was set to 15 °C min^{-1}. SEC measurements were realized using a Tosoh Bioscience HLC-8321 GPC/HT instrument equipped with a TSKgel GMHHR-H(20)-HT2 column. 1,2,4-Trichlorobenzene (TCB) was used as the eluent at 110 °C. The apparatus was calibrated using monodisperse polystyrene standards. All materials were solubilized (1 mg mL^{-1}) under agitation in TCB at 60 °C for 1 hour to ensure complete solubilization of the aggregates. Then, the samples were filtered through a 0.45 μm glass microfibre filter into a 5 mL chromatography vial. All vials were kept at 110 °C before their injection into the apparatus. The microwave synthesis reactor was an Anton Paar Monowave 300. X-ray powder diffractograms were obtain on a Rigaku Mini-Flex 600. Cu-Kα radiation (λ = 1.5406 Å) was used as X-ray source. The XRD pattern has been taken from 3° to 90° 2θ range with scan rate of 10° per minute on a thin film drop-casted from a polymer solution in $CHCl_3$ on silicon substrate.

Computational method

Geometry optimization and frequency calculations were carried out using the Gaussian-16 (Revision C.01) suite of programs.[52] All calculations were performed at the B3LYP/TZVP (except DZVP for palladium) level of theory with a superfine integration grid.[53–56] To minimize computational cost without greatly influencing the accuracy of the results, alkoxy side chains (–$OCH_2CH(C_6H_{13})(C_8H_{17})$) were simplified as methoxy (–OCH_3) for the monomer M2. In a similar fashion, the simplified catalyst model, (PMe_3)Pd(Ph)(CH_3COO^-), was used for every CMD transition state calculation (Fig. 2).[57] Every structure went through a conformation analysis in order to find its global minima and the lowest energy transition state possible. Frequency calculations were performed to confirm that each optimized structure corresponded to a true minimum on the potential energy surface, ensuring the absence of any imaginary frequencies. For transition state structures, frequency analysis confirmed the presence of exactly one imaginary frequency. Free energies were calculated at 298 K and 1 atm.

OSCs device fabrication details

Devices were fabricated using commercial ITO-coated glass substrates (10 Ω per square, Thin Film Devices). The substrates were cleaned using cleanroom detergent, water, acetone, and isopropyl alcohol. The wet-cleaned ITO-glass substrates were subject to a plasma-oxygen treatment for 5 minutes. The sol–gel ZnO was then spin-coated on the ITO and treated at 200 °C for 10 minutes. The PDTBTBz-2F$_{anti}$:$PC_{61}BM$ solutions were spin-coated onto the ZnO-coated ITO-glass substrates at room temperature, with a spin rate of 2000 rpm. The active layer solution was formed from a 1 : 1.5 D : A weight ratio in a 16 mg mL^{-1} polymer concentration. Chlorobenzene was added to the materials, and the solution was stirred for 2h at 60 °C. 2% v/v diphenyl ether (DPE) was added 1 hour prior to the solution deposition. After the solution deposition, a MoO_3 layer (10 nm) and an Ag one (80 nm) were subsequently deposited onto the BHJ layer using high-vacuum techniques. The current density–voltage curves (J–V) were measured using a Kethley 2400 source meter on an active area of 0.09 cm^2. The solar cells (with no protective encapsulation) were then tested in air under an AM 1.5 spectrum produced with a light intensity of 100 mW cm^{-2} from an Oriel instruments Solar Simulator.

Conflicts of interest

The authors declare no competing financial interests.

Data availability

The data supporting the findings of this study can be found in the supplementary information (SI). Supplementary information: synthesis of the monomers and polymers, UV-vis spectra of the polymer, cyclic voltammograms of the polymers, X-ray diffractograms, thermogravimetric analysis and differential scanning calorimetry of the polymers ^{1}H and ^{13}C NMR of the intermediates and the ^{1}H NMR of the polymers, as well as organic solar cells measurements and conditions for flow synthesis. See DOI: https://doi.org/10.1039/d5py00957j.

Acknowledgements

The authors acknowledge the Fonds de Recherche du Québec, Nature et Technologies (FRQNT) grants #293062 and #325901, for financial support. Calculations were performed on the Digital Alliance of Canada Cedar cluster.

Paul A. Johnson was supported by NSERC grant #RGPIN-2024-05610.

References

1 A. G. S. Al-Azzawi, S. B. Aziz, E. M. A. Dannoun, A. Iraqi, M. M. Nofal, A. R. Murad and A. M. Hussein, *Polymers*, 2023, **15**, 164.
2 T. Kotnik and S. Kovačič, *Eur. J. Org. Chem.*, 2025, e202400874.
3 L. Giraud, S. Grelier, E. Grau, G. Hadziioannou, C. Brochon, H. Cramail and E. Cloutet, *J. Mater. Chem. C*, 2020, **8**, 9792–9810.
4 L. Giraud, S. Grelier, E. Grau, L. Garel, G. Hadziioannou, B. Kauffmann, É. Cloutet, H. Cramail and C. Brochon, *Molecules*, 2022, **27**, 4138.
5 L.-P. Boivin, W. Dupont, D. Gendron and M. Leclerc, *Macromol. Chem. Phys.*, 2023, **224**, 2200378.
6 W. Shin, W. Ko, S.-H. Jin, T. Earmme and Y.-J. Hwang, *Chem. Eng. J.*, 2021, **412**, 128572.
7 S. M. Lee, K. H. Park, S. Jung, H. Park and C. Yang, *Nat. Commun.*, 2018, **9**, 1867.
8 O. Beckers, S. Smeets, L. Lutsen and W. Maes, *J. Mater. Chem. C*, 2022, **10**, 1606–1616.
9 N. S. Gobalasingham, J. E. Carlé, F. C. Krebs, B. C. Thompson, E. Bundgaard and M. Helgesen, *Macromol. Rapid Commun.*, 2017, **38**, 1700526.
10 Y. Kim, C. Lee, D. Seo, D. Kim, F. S. Kim, G. I. Peterson and Y.-J. Hwang, *Chem. Eng. J.*, 2024, **480**, 148016.
11 M. B. Plutschack, B. Pieber, K. Gilmore and P. H. Seeberger, *Chem. Rev.*, 2017, **117**, 11796–11893.
12 Y.-J. You, C. E. Song, Q. V. Hoang, Y. Kang, J. S. Goo, D.-H. Ko, J.-J. Lee, W. S. Shin and J. W. Shim, *Adv. Funct. Mater.*, 2019, **29**, 1901171.
13 L.-P. Boivin, W. Dupont, M. Leclerc and D. Gendron, *J. Org. Chem.*, 2021, **86**, 16548–16557.
14 W. Dupont, L.-P. Boivin, M. Mainville, Y. Yuan, Y. Li, M. Leclerc and D. Gendron, *ACS Appl. Polym. Mater.*, 2025, **7**, 29–41.
15 L.-P. Boivin, M. Prud'homme, A. Poitras, W. Dupont, M. Leclerc and D. Gendron, *New J. Chem.*, 2025, **49**, 13089–13097.
16 S.-J. Ko, Q. V. Hoang, C. E. Song, M. A. Uddin, E. Lim, S. Y. Park, B. H. Lee, S. Song, S.-J. Moon, S. Hwang, P.-O. Morin, M. Leclerc, G. M. Su, M. L. Chabinyc, H. Y. Woo, W. S. Shin and J. Y. Kim, *Energy Environ. Sci.*, 2017, **10**, 1443–1455.
17 A. L. Mayhugh, P. Yadav and C. K. Luscombe, *J. Am. Chem. Soc.*, 2022, **144**, 6123–6135.
18 M. Leclerc, S. Brassard and S. Beaupré, *Polym. J.*, 2020, **52**, 13–20.
19 S. Brassard, M. H. Sangachin and M. Leclerc, *Macromolecules*, 2023, **56**, 1362–1371.
20 J. T. Blaskovits, P. A. Johnson and M. Leclerc, *Macromolecules*, 2018, **51**, 8100–8113.
21 B. Liégault, D. Lapointe, L. Caron, A. Vlassova and K. Fagnou, *J. Org. Chem.*, 2009, **74**, 1826–1834.
22 T. Bura, S. Beaupré, M.-A. Légaré, J. Quinn, E. Rochette, J. T. Blaskovits, F.-G. Fontaine, A. Pron, Y. Li and M. Leclerc, *Chem. Sci.*, 2017, **8**, 3913–3925.
23 F. Grenier, B. R. Aïch, Y.-Y. Lai, M. Guérette, A. B. Holmes, Y. Tao, W. W. H. Wong and M. Leclerc, *Chem. Mater.*, 2015, **27**, 2137–2143.
24 M. Mainville, V. Tremblay, M. Z. Fenniri, A. Laventure, M. E. Farahat, R. Ambrose, G. C. Welch, I. G. Hill and M. Leclerc, *Asian J. Org. Chem.*, 2020, **9**, 1318–1325.
25 F. Grenier, K. Goudreau and M. Leclerc, *J. Am. Chem. Soc.*, 2017, **139**, 2816–2824.
26 S. Hayashi, *Mater. Adv.*, 2020, **1**, 632–638.
27 Z. Chu, H. Guo, W. Yu, Z. Sun and W. Chen, *J. Polym. Sci.*, 2024, **62**, 4270–4276.
28 Y.-Y. Zhou, Z.-Y. Wang, Z.-F. Yao, Z.-D. Yu, Y. Lu, X.-Y. Wang, Y. Liu, Q.-Y. Li, L. Zou, J.-Y. Wang and J. Pei, *CCS Chem.*, 2021, **3**, 2994–3004.
29 T. Bura, P.-O. Morin and M. Leclerc, *Macromolecules*, 2015, **48**, 5614–5620.
30 S. Sabury, Z. Xu, S. Saiev, D. Davies, A. M. Österholm, J. M. Rinehart, M. Mirhosseini, B. Tong, S. Kim, J.-P. Correa-Baena, V. Coropceanu, O. D. Jurchescu, J.-L. Brédas, Y. Diao and J. R. Reynolds, *Mater. Horiz.*, 2024, **11**, 3352–3363.
31 L. D. A. Siebbeles, F. C. Grozema, M. P. de Haas and J. M. Warman, *Radiat. Phys. Chem.*, 2005, **72**, 85–91.
32 M. Chayer, K. Faïd and M. Leclerc, *Chem. Mater.*, 1997, **9**, 2902–2905.
33 G. H. L. Heintges, K. H. Hendriks, F. J. M. Colberts, M. Li, J. Li and R. A. J. Janssen, *RSC Adv.*, 2019, **9**, 8740–8747.
34 S. Sabury, A. L. Jones, N. Schopp, S. Nanayakkara, T. P. Chaney, V. Coropceanu, S. R. Marder, M. F. Toney, J.-L. Brédas, T.-Q. Nguyen and J. R. Reynolds, *Chem. Mater.*, 2024, **36**, 11656–11668.
35 R. E. Aderne, B. G. A. L. Borges, H. C. Ávila, F. von Kieseritzky, J. Hellberg, M. Koehler, M. Cremona,

L. S. Roman, C. M. Araujo, M. L. M. Rocco and C. F. N. Marchiori, *Mater. Adv.*, 2022, **3**, 1791–1803.
36 S. Hayashi, *Mater. Adv.*, 2020, **1**, 632–638.
37 S.-H. Peng, W.-Y. Tu, G. Gollavelli and C.-S. Hsu, *Polym. Chem.*, 2017, **8**, 3431–3437.
38 F. Livi, N. S. Gobalasingham, B. C. Thompson and E. Bundgaard, *J. Polym. Sci., Part A: Polym. Chem.*, 2016, **54**, 2907–2918.
39 W. Wang, Q. Wu, R. Sun, J. Guo, Y. Wu, M. Shi, W. Yang, H. Li and J. Min, *Joule*, 2020, **4**, 1070–1086.
40 M.-H. Jao, H.-C. Liao and W.-F. Su, *J. Mater. Chem. A*, 2016, **4**, 5784–5801.
41 V. S. Balderrama, F. Ávila-Herrera, J. G. Sánchez, J. Pallarès, O. Vigil-Galán, L. F. Marsal and M. Estrada, *IEEE J. Photovoltaics*, 2016, **6**, 491–497.
42 N. R. Kakde, H. J. Bharathkumar, B. A. Wavhal, A. Nikam, S. Patil, S. R. Dash, K. Vanka, K. Krishnamoorthy, A. Kulkarni and S. K. Asha, *J. Mater. Chem. C*, 2022, **10**, 13025–13039.
43 H. Seyler, D. J. Jones, A. B. Holmes and W. W. H. Wong, *Chem. Commun.*, 2012, **48**, 1598–1600.
44 L. Konermann, *J. Phys. Chem. A*, 1999, **103**, 7210–7216.
45 O. Beckers, S. Gielen, F. Verstraeten, P. Verstappen, L. Lutsen, K. Vandewal and W. Maes, *ACS Appl. Polym. Mater.*, 2020, **2**, 4373–4378.
46 T. Yamada, J. Jiang, N. Ito, K. Park, H. Masuda, C. Furugen, M. Ishida, S. Ōtori and H. Sajiki, *Catalysts*, 2020, **10**, 1209.
47 D. Tsaoulidis and P. Angeli, *AIChE J.*, 2016, **62**, 315–324.
48 R. K. Verma and S. Ghosh, *ChemBioEng Rev.*, 2019, **6**, 5–16.
49 T. von Keutz, D. Cantillo and C. O. Kappe, *J. Flow Chem.*, 2019, **9**, 27–34.
50 A. Etminan, Y. S. Muzychka and K. Pope, *Processes*, 2021, **9**, 870.
51 J.-R. Pouliot, F. Grenier, J. T. Blaskovits, S. Beaupré and M. Leclerc, *Chem. Rev.*, 2016, **116**, 14225–14274.
52 M. J. Frisch, G. W. Trucks, H. B. Schlegel, G. E. Scuseria, M. A. Robb, J. R. Cheeseman, G. Scalmani, V. Barone, G. A. Petersson, H. Nakatsuji, X. Li, M. Caricato, A. V. Marenich, J. Bloino, B. G. Janesko, R. Gomperts, B. Mennucci, H. P. Hratchian, J. V. Ortiz, A. F. Izmaylov, J. L. Sonnenberg, D. Williams-Young, F. Ding, F. Lipparini, F. Egidi, J. Goings, B. Peng, A. Petrone, T. Henderson, D. Ranasinghe, V. G. Zakrzewski, J. Gao, N. Rega, G. Zheng, W. Liang, M. Hada, M. Ehara, K. Toyota, R. Fukuda, J. Hasegawa, M. Ishida, T. Nakajima, Y. Honda, O. Kitao, H. Nakai, T. Vreven, K. Throssell, J. A. Montgomery Jr., J. E. Peralta, F. Ogliaro, M. J. Bearpark, J. J. Heyd, E. N. Brothers, K. N. Kudin, V. N. Staroverov, T. A. Keith, R. Kobayashi, J. Normand, K. Raghavachari, A. P. Rendell, J. C. Burant, S. S. Iyengar, J. Tomasi, M. Cossi, J. M. Millam, M. Klene, C. Adamo, R. Cammi, J. W. Ochterski, R. L. Martin, K. Morokuma, O. Farkas, J. B. Foresman and D. J. Fox, 2016.
53 C. Lee, W. Yang and R. G. Parr, *Phys. Rev. B: Condens. Matter Mater. Phys.*, 1988, **37**, 785–789.
54 A. D. Becke, *J. Chem. Phys.*, 1993, **98**, 5648–5652.
55 A. Schäfer, C. Huber and R. Ahlrichs, *J. Chem. Phys.*, 1994, **100**, 5829–5835.
56 N. Godbout, D. R. Salahub, J. Andzelm and E. Wimmer, *Can. J. Chem.*, 1992, **70**, 560–571.
57 S. I. Gorelsky, D. Lapointe and K. Fagnou, *J. Org. Chem.*, 2012, **77**, 658–668.